



Deposited via The University of Leeds.

White Rose Research Online URL for this paper:

<https://eprints.whiterose.ac.uk/id/eprint/1198/>

---

**Article:**

Gaskell, P.H., Savage, M.D. and Wilson, M. (1997) Stokes flow in a half-filled annulus between rotating coaxial cylinders. *Journal of Fluid Mechanics*, 337. pp. 263-282. ISSN: 1469-7645

---

**Reuse**

See Attached

**Takedown**

If you consider content in White Rose Research Online to be in breach of UK law, please notify us by emailing [eprints@whiterose.ac.uk](mailto:eprints@whiterose.ac.uk) including the URL of the record and the reason for the withdrawal request.

## Stokes flow in a half-filled annulus between rotating coaxial cylinders

By P. H. GASKELL<sup>1</sup>, M. D. SAVAGE<sup>2</sup> AND M. WILSON<sup>3</sup>

<sup>1</sup>Department of Mechanical Engineering,

<sup>2</sup>Department of Physics and Astronomy,

<sup>3</sup>Department of Applied Mathematical Studies,  
University of Leeds, Leeds, LS2 9JT, UK

(Received 25 October 1995 and in revised form 12 December 1996)

A model is presented for viscous flow in a cylindrical cavity (a half-filled annulus lying between horizontal, infinitely long concentric cylinders of radii  $R_i, R_o$ , rotating with peripheral speeds  $U_i, U_o$ ). Stokes' approximation is used to formulate a boundary value problem which is solved for the streamfunction,  $\psi$ , as a function of radius ratio  $\bar{R} = R_i/R_o$  and speed ratio  $S = U_i/U_o$ .

Results show that for  $S > 0$  ( $S < 0$ ) the flow domain consists of two (one) large eddies (eddy), each having a stagnation point on the centreline and a potentially rich substructure with separatrices and sub-eddies. The behaviour of the streamfunction solution in the neighbourhood of stagnation points on the centreline is investigated by means of a truncated Taylor expansion. As  $\bar{R}$  and  $S$  are varied it is shown that a bifurcation in the flow structure arises in which a centre becomes a saddle stagnation point and vice versa. As  $\bar{R} \rightarrow 1$ , a sequence of 'flow bifurcations' leads to a flow structure consisting of a set of nested separatrices, and provides the means by which the two-dimensional cavity flow approaches quasi-unidirectional flow in the small gap limit. Control-space diagrams reveal that speed ratio has little effect on the flow structure when  $S < 0$  and also when  $S > 0$  and aspect ratios are small (except near  $S = 1$ ). For  $S > 0$  and moderate to large aspect ratios the bifurcation characteristics of the two large eddies are quite different and depend on both  $\bar{R}$  and  $S$ .

---

### 1. Introduction

Investigation of the flow in a fluid-filled annulus lying between rotating concentric cylinders began with the work of Couette (1890), giving rise to what is termed Couette flow. Taylor (1923) studied the centrifugal instability associated with this type of flow and showed the existence of axisymmetric vortices when the Taylor number exceeds a critical value. Similar vortices are found to occur between concentric cylinders when the flow is driven by an azimuthal pressure gradient, Dean (1928).

Flow in a partially filled annulus lying between horizontal rotating concentric cylinders (the 'Taylor–Dean' system) represents a combination of the above two types of flow and was first studied theoretically by Brewster, Grosberg & Nissan (1959). Recently the formation and stability of various secondary flows in this system has been the subject of a number of papers – see, for example, Mutabazi & Andreck (1991) and Mutabazi *et al.* (1988, 1989) for experimental and theoretical investigations

of stationary and time-dependent flow patterns, and Chen & Chang (1992) for a study of non-axisymmetric modes of instability.

The present work is not concerned with these stability phenomena, but rather with the existence of recirculating eddies and local bifurcations in the two-dimensional steady base flow for the case when the annulus is half-filled. Such a configuration is used in the steel galvanizing plants described by Komoda (1983) and Nabatame (1984), and has been studied both experimentally and theoretically by Chen *et al.* (1990) for Reynolds number  $Re \geq 67$ . Their approach was to split the domain into 'end' and 'core' regions in which the governing equations were expanded as a power series in the annulus aspect ratio. In the core region the flow field was assumed to be independent of the azimuthal coordinate, and hence independent of Reynolds number. The zero- and first-order equations in the end regions were solved with non-zero  $Re$  using a finite difference scheme. At the end of their paper they remarked that obtaining a solution for  $Re \rightarrow 0$  was the subject of further work, but the present authors are unaware of this having been published.

The work of Chen *et al.* (1990) is complemented by that of Normand, Mutabazi & Wesfreid (1991), who investigated the base flow in a partially filled annulus in the neighbourhood of the free surfaces. They used linear stability analysis to show the existence of recirculations near one or both free surfaces, depending on the relative rotation rates of the cylinders. Of relevance to the present study is the result that such eddies can exist even in the limit of zero Reynolds number.

Jeffrey & Sherwood (1980) studied the streamline patterns of various two-dimensional Stokes flows, particularly those with eddies or regions of closed streamlines. They considered ways in which a flow may be turned back on itself or 'blocked' and showed the presence of centres and saddle points, but did not examine the transition from one to the other.

Stokes flow in a rectangular cavity driven by the uniform motion of one of its lids has been studied by several authors. Recently Shankar (1993) investigated the role of corner eddies in the generation of large-eddy structures seen in this flow. Particular attention was paid to the error induced by truncation of the eigenfunction solution, and two previous papers (Pan & Acrivos 1967; Joseph & Sturges 1978) were shown to contain quantitative inaccuracies. In the case of the former, these errors were due to the use of an insufficiently refined finite difference grid, whereas the latter employed too few eigenfunctions in their biorthogonal series expansion.

Jana, Metcalfe & Ottino (1994) considered Stokes flow in two quite different cavity systems: a rectangular cavity with two moving lids, and the cavity formed between two cylinders positioned inside, and symmetrically along the diameter of a third. They discussed the possible steady flow structures that exist in each case and considered the mixing effect produced by moving the boundaries following a periodic piecewise steady 'protocol'.

Steady Stokes flow in an annular cavity driven by rotating cylinders has been investigated recently by Krasnopolskaya *et al.* (1996). Their paper outlines a solution procedure involving the superposition of two Fourier series to satisfy all the boundary conditions. The coefficients in each infinite expansion depend on all the coefficients in the other, and so the issue of accuracy and convergence in the truncated system is addressed. They examine the asymptotic behaviour of the Fourier coefficients and derive accurate and computationally efficient formulae for the numerical evaluation of streamfunction and velocity. The technique is illustrated by a number of examples where the effect of cylinder speed ratio on flow structure is investigated. The flow is seen to contain one or two main recirculations depending on the sign of the speed

ratio. When one of the cylinders is at rest, Moffatt eddies (Moffatt 1964) are seen, but as the stationary cylinder is set in motion these disappear, and the primary corner eddies become internal eddies enclosed by a separatrix which passes through a saddle point on the centreline. As the speed ratio increases, the centres of the two eddies approach the saddle and coalesce to leave a single eddy. These flow features and transformations (and many others) also exist in the rectangular double lid-driven cavity and have been described in detail by Gurcan (1996).

Although the geometry of the present problem is similar to that considered by Krasnopolskaya *et al.* (1996), the solution is much simpler, since the boundary conditions on the liquid–gas interfaces are such that only a single Fourier series is required and the form of the coefficients allows the Shanks transformation (Bender & Orszag 1978) to be used to accelerate convergence.

Flow in a rectangular cavity with two free surfaces and driven by two moving plates was formulated by Thompson (1992) and Gaskell *et al.* (1995) to model the flow within a small liquid bead located between two rotating rolls, typical of the problems observed in meniscus roll coating. The model treats the rolls as flat plates and the meniscus at each end of the bead as a plane surface of zero shear stress. It was found that at certain values of the control parameters the flow contained a saddle point whereas at others only a centre was present. This change in flow structure was observed in both forward and reverse roll coating as aspect ratio and speed ratio were changed, Gaskell, Innes & Savage (1996). Gurcan (1996) has used Thompson's idealized model to investigate the flow structure further by considering the behaviour of the streamfunction close to stagnation points.

It is the aim of the present paper to provide a complete zero-Reynolds-number solution for the geometry considered by Chen *et al.* (1990) and to use the approach of Gurcan to study the effects of annulus aspect ratio, speed ratio, and curvature on the structure of the flow.

## 2. Formulation of the model

The geometry under investigation is shown in figure 1. A Newtonian liquid, of constant density  $\rho$  and viscosity  $\mu$ , half-fills the annulus between two horizontal, infinitely long concentric cylinders of radii  $R_i$  and  $R_o$ , where subscripts  $i$  and  $o$  indicate 'inner' and 'outer' respectively. The flow is driven by the motion of the cylinders, which are allowed to rotate independently with peripheral speeds  $U_i$  and  $U_o$  in either the same or opposite direction. The cylinder speeds are assumed to be slow so that the creeping flow approximation holds. When the cylinders are stationary the liquid exactly half-fills the annulus and it is assumed that, as in the experiments of Chen *et al.* (1990), the cylinders dewet as they rotate, such that no liquid films are withdrawn from the bulk. Thus there are four three-phase contact lines and the liquid domain is closed.

The pressure field developed by the motion of the cylinders must support a pressure head of height  $\Delta h$ , measured between the centres of the two interfaces. In the small gap limit, lubrication theory gives the pressure gradient as

$$\frac{2}{(R_o + R_i)} \frac{dp}{d\theta} = \frac{6\mu(U_i + U_o)}{(R_o - R_i)^2},$$

which leads to the balance

$$\rho g \Delta h = \frac{6\mu(U_i + U_o)}{(R_o - R_i)^2} \frac{(R_o + R_i)}{2} \pi,$$

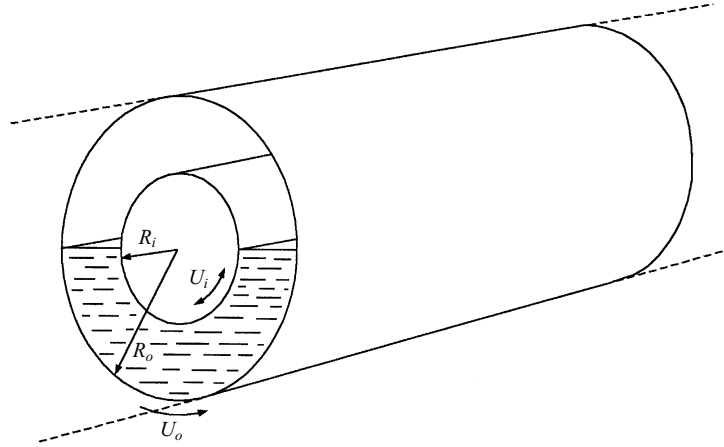


FIGURE 1. The flow geometry.

where  $g$  is the acceleration due to gravity. The free surfaces are therefore modelled as radial planes inclined at an angle

$$\alpha = \sin^{-1} \frac{\Delta h}{R_i + R_o} = \sin^{-1} \left( \frac{3\mu\pi(U_i + U_o)}{\rho g(R_o - R_i)^2} \right) \quad (2.1)$$

to the horizontal. The normal stress condition must then be relaxed while the kinematic and shear stress conditions can be applied on the plane. The flow is taken to be steady, and since for this to be true  $\alpha$  must be less than  $\pi/2$ , expression (2.1) shows that the cylinders must be rotated sufficiently slowly for a given geometry. The flow is also assumed to be two-dimensional, and the plane  $\theta = 0$  is taken as the centre of the liquid half-annulus such that the interfaces lie along  $\theta = \pm\pi/2$ . The assumptions are summarized as follows,

- (a) The liquid domain is closed, and the flux past any line  $\theta = \text{constant}$  is zero.
- (b) The flow is two-dimensional and steady, with inertial effects assumed to be negligible.
- (c) The free surfaces are represented by radial planes, on which shear stress vanishes.

Under the Stokes approximation, the equations of motion reduce to the biharmonic equation for the streamfunction,  $\Psi$ , which in polar coordinates  $(R, \theta)$  is

$$\nabla^4 \Psi = \left( \frac{\partial^2}{\partial R^2} + \frac{1}{R} \frac{\partial}{\partial R} + \frac{1}{R^2} \frac{\partial^2}{\partial \theta^2} \right)^2 \Psi = 0. \quad (2.2)$$

If the following non-dimensional variables are introduced:

$$\mathbf{u} = \frac{\mathbf{U}}{U_o}, \quad r = \frac{R}{R_o}, \quad \psi = \frac{\Psi}{U_o R_o},$$

the radial and tangential velocity components are given by

$$u_r = \frac{1}{r} \frac{\partial \psi}{\partial \theta} \quad \text{and} \quad u_\theta = -\frac{\partial \psi}{\partial r}. \quad (2.3)$$

The two control parameters are the radius and speed ratios of the cylinders:

$$\bar{R} = \frac{R_i}{R_o}, \quad S = \frac{U_i}{U_o}.$$

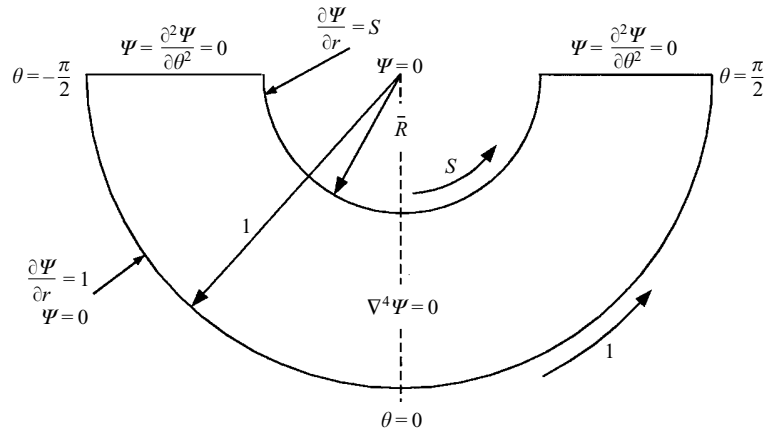


FIGURE 2. The boundary value problem.

2.1. Boundary conditions

Assuming no slip on the cylinder surfaces

$$\frac{\partial \psi}{\partial r} = 1 \text{ on } r = 1, \quad \text{and} \quad \frac{\partial \psi}{\partial r} = S \text{ on } r = \bar{R}. \tag{2.4}$$

The balance of shear stress at a planar liquid-gas interface where the viscosity of the gas is negligible reduces to

$$\boldsymbol{\sigma} \cdot \mathbf{n} = 0,$$

where

$$\boldsymbol{\sigma} = -p\mathbf{I} + \mu[\nabla\mathbf{u} + (\nabla\mathbf{u})^T],$$

is the stress tensor of the liquid, and  $\mathbf{n}$  is the outward-pointing normal to the plane. ( $p$  is the pressure and  $\mathbf{I}$  is the unit tensor). Since  $u_\theta \equiv 0$  on  $\theta = \pm\pi/2$ , this condition reduces to

$$\frac{\partial^2 \psi}{\partial \theta^2} = 0 \quad \text{on } \theta = \pm\frac{1}{2}\pi. \tag{2.5}$$

As there is no flux through any of the boundaries, the streamfunction must be constant and for simplicity is taken to be zero:

$$\psi = 0 \quad \text{on } r = \bar{R}, r = 1, \theta = \pm\frac{1}{2}\pi. \tag{2.6}$$

The complete boundary value problem is illustrated in figure 2.

3. Method of solution

3.1. Streamfunction solution

An even solution to (2.2) is sought of the form

$$\psi \sim f(r) \cos \lambda\theta. \tag{3.1}$$

Condition (2.5) requires that  $\cos \lambda\pi/2 = 0$  for all  $\lambda$ , hence the eigenvalues are given by

$$\lambda_n = (2n - 1) \quad \text{for } n = 1, 2, \dots, \tag{3.2}$$

so that

$$\psi \sim \sum f_n(r) \cos \lambda_n \theta. \tag{3.3}$$

Substitution of (3.1) into (2.2) yields the general form of the functions  $f_n(r)$ :

$$f_n(r) = A_n r^{\lambda_n} + B_n r^{-\lambda_n} + C_n r^{2+\lambda_n} + D_n r^{2-\lambda_n}, \tag{3.4}$$

where  $A_n, \dots, D_n$  are real coefficients. This is equivalent to the first of the two Fourier series used by Krasnopolskaya *et al.* (1996); however those authors did not point out that for  $n = 1$  a repeated root occurs in (3.4), since the functions  $r^{\lambda_1}$  and  $r^{2-\lambda_1}$  are identical. The fourth independent solution is  $r \ln r$ , and therefore

$$f_1(r) = A_1 r + B_1 r^3 + C_1 r^{-1} + D_1 r \ln r. \tag{3.5}$$

Here only one series is needed since the ‘natural’ boundary conditions on  $\theta = \pm\pi/2$  are both satisfied by the form of the eigenvalues (3.2) and there remain two conditions on each cylinder to determine the coefficients  $A_n, \dots, D_n$ . Since  $\psi = 0$  on  $r = \bar{R}$  and  $r = 1$ , two sets of coefficients in (3.4) and (3.5) can be eliminated. The general solution for the streamfunction is then expressed as

$$\begin{aligned} \psi = & \left[ A_1 \left\{ r - r^3 - (1 - \bar{R}^2) \frac{r \ln r}{\ln \bar{R}} \right\} + B_1 \left\{ r^{-1} - r^3 - (\bar{R}^{-1} - \bar{R}^3) \frac{r \ln r}{\bar{R} \ln \bar{R}} \right\} \right] \cos \theta \\ & + \sum_{n=2}^{\infty} \left[ A_n \left\{ r^{2n-1} - r^{3-2n} - (\bar{R}^{2n-1} - \bar{R}^{3-2n}) \left( \frac{r^{2n+1} - r^{3-2n}}{\bar{R}^{2n+1} - \bar{R}^{3-2n}} \right) \right\} \right. \\ & \left. + B_n \left\{ r^{1-2n} - r^{3-2n} - (\bar{R}^{1-2n} - \bar{R}^{3-2n}) \left( \frac{r^{2n+1} - r^{3-2n}}{\bar{R}^{2n+1} - \bar{R}^{3-2n}} \right) \right\} \right] \cos(2n - 1)\theta. \tag{3.6} \end{aligned}$$

The remaining coefficients are found from the no-slip conditions on the cylindrical surfaces:

$$\begin{aligned} A_1 = & \frac{1}{\pi} \left[ \frac{(S - 1)(1 - \bar{R}^4) + 2(2S\bar{R}^2 - \bar{R}^4 - 1) \ln \bar{R}}{(1 - \bar{R})(1 + \bar{R})(1 - \bar{R}^2 + (1 + \bar{R}^2) \ln \bar{R})} \right], \\ B_1 = & \frac{1}{\pi} \left[ \frac{\bar{R}^2[(S - 1)(1 - \bar{R}^2) + 2(S - \bar{R}^2) \ln \bar{R}]}{(\bar{R} - 1)(1 + \bar{R})(1 - \bar{R}^2 + (1 + \bar{R}^2) \ln \bar{R})} \right], \\ A_n = & \frac{1}{\pi} \frac{(-1)^{n+1}}{(2n - 1)} \left[ \frac{(S - 1)\bar{R}^2(1 + \bar{R}^{-2n})}{-\bar{R}^{2n} - (2n - 1)(\bar{R}^2 - 1) + \bar{R}^{2-2n}} + \frac{(S + 1)\bar{R}^2(1 - \bar{R}^{-2n})}{-\bar{R}^{2n} + (2n - 1)(\bar{R}^2 - 1) + \bar{R}^{2-2n}} \right], \\ B_n = & \frac{1}{\pi} \frac{(-1)^{n+1}}{(2n - 1)} \left[ \frac{(1 - S)(\bar{R}^{2n} + \bar{R}^2)}{-\bar{R}^{2n} - (2n - 1)(\bar{R}^2 - 1) + \bar{R}^{2-2n}} + \frac{(S + 1)(\bar{R}^{2n} - \bar{R}^2)}{-\bar{R}^{2n} + (2n - 1)(\bar{R}^2 - 1) + \bar{R}^{2-2n}} \right]. \end{aligned}$$

### 3.2. Convergence to boundary values

Expression (3.6) satisfies (2.6) exactly, but it is important to assess the number of terms required to achieve a given accuracy in the streamfunction and velocity at any point in the domain. It is found that for both the streamfunction and velocity more terms are needed near the cylinder surfaces than elsewhere in the domain – to obtain two-decimal-place accuracy 100 terms are necessary near the cylinder surfaces whereas in the core of the domain 20 terms suffice. Convergence of both series can be improved dramatically throughout the domain by use of the Shanks transformation

$n$	$P_n$	$S(P_n)$	$S^2(P_n)$	$S^3(P_n)$
1	1.27323954	-	-	-
2	0.84882636	1.00798131	-	-
3	1.10347427	0.99737098	1.00016317	-
4	0.92158291	1.00116038	0.99995466	1.00000213
5	1.06305397	0.99939199	1.00001613	0.99999943
6	0.94730492	1.00035657	0.99999319	1.00000018
7	1.04524642	0.99977358	1.00000324	0.99999993
8	0.96036379	1.00015252	0.99999830	1.00000003
9	1.03526023	0.99989247	1.00000096	0.99999999
10	0.96824762	1.00007861	0.99999943	1.00000001
⋮	⋮			
100	0.99681698			

TABLE 1. The effect of repeated application of the Shanks transformation on the convergence of  $\partial\psi/\partial r$  at  $r = \bar{R}$  for  $\bar{R} = 0.7$  and  $S = 1.0$

(Bender & Orszag 1978)

$$S(P_n) = \frac{P_{n+1}P_{n-1} - P_n^2}{P_{n+1} + P_{n-1} - 2P_n} = P_n - \frac{(P_{n+1} - P_n)(P_n - P_{n-1})}{(P_{n+1} - P_n) - (P_n - P_{n-1})}, \tag{3.7}$$

on the sequence  $P_n$  of partial sums. Repeated application of (3.7) generates new and even more rapidly converging sequences. The effect of (3.7) is illustrated in table 1 where the convergence of  $\partial\psi/\partial r$  at  $r = \bar{R}$  is considered.

It remains then to determine the number of applications of (3.7) required to ensure a given accuracy. As will be seen later, an accuracy of 10 decimal places is necessary in the interior of the domain to determine flow features near stagnation points. Insisting that the streamfunction and velocity are known to this accuracy near the cylinder surfaces will therefore guarantee at least this level of accuracy throughout the domain. This is achieved by taking 30 terms in the sequence generated by 8 Shanks transformations.

### 3.3. Location of stagnation points

*Stagnation points lying on  $\theta = 0$*

Examples of streamline patterns are given in figures 3–6 for both co-rotating ( $S > 0$ ) and contra-rotating ( $S < 0$ ) cylinders and show that, as expected, there are either one or two stagnation points on the line  $\theta = 0$ , according to whether  $S < 0$  or  $S > 0$ . In the next section an expansion about these stagnation points is used to determine the local behaviour of the solution and so the corresponding radial position must be found. The velocity components are given in terms of the streamfunction by (2.3) and clearly the radial velocity vanishes on the the line  $\theta = 0$ . Since the azimuthal velocity component has opposite sign on either side of a stagnation point a bisection method can be used to determine the radial position of that point. The velocity component  $\partial\psi/\partial r$  is evaluated at a number of points along  $\theta = 0$  and any interval having  $\partial\psi/\partial r$  opposite in sign at its extremes is successively bisected so as to approach the value(s) of  $r$  where  $\partial\psi/\partial r = 0$ .

*Analytical approximation*

It is assumed that, for a small enough gap, the flow in the core region, away from the free surfaces, is purely azimuthal, and the pressure gradient  $\partial p/\partial\theta$ , is constant.

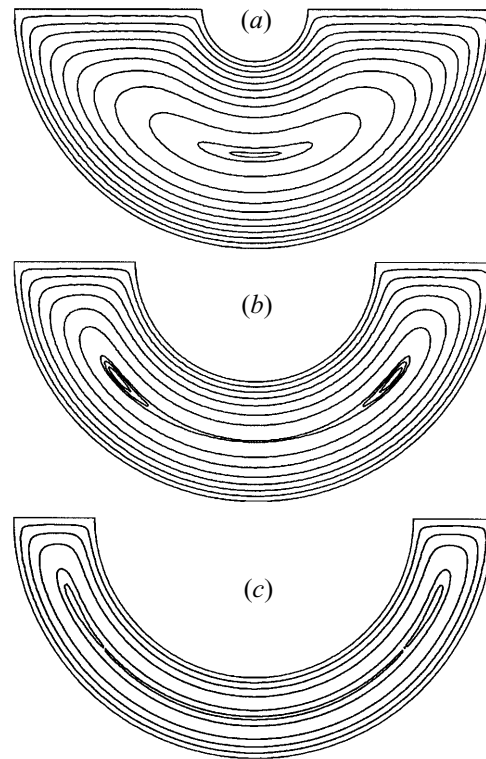


FIGURE 3. Streamline patterns for  $S = -1$  and various  $\bar{R}$ :  
 (a)  $\bar{R} = 0.222$ ; (b)  $\bar{R} = 0.5$ ; (c)  $\bar{R} = 0.67$ .

The velocity distribution is thus

$$v(r) = Ar \ln r + Br + C/r, \quad (3.8)$$

where  $A = \frac{1}{2}(\partial p/\partial \theta)$  is found from the zero flux condition  $\int_{r=\bar{R}}^{r=1} V(r) dr = 0$  and  $B$  and  $C$  are determined from the boundary conditions on the cylinders. However, in the limit  $\bar{R} \rightarrow 1$  a simpler, quadratic velocity distribution may be derived:

$$v(\bar{Y}) = 3(S + 1)\bar{Y}^2 - 2(2S + 1)\bar{Y} + S, \quad (3.9)$$

where  $\bar{Y} = (r - \bar{R})/(1 - \bar{R})$ . This velocity vanishes at either one or two values of  $\bar{Y} \in (0, 1)$ , according to whether  $S < 0$ , figure 3, or  $S > 0$ , figure 5, and can easily be solved for stagnation lines. The derivation of (3.9) neglects the curvature of the domain since no distinction is made between the radii of the cylinders. Solving (3.8) by Newton–Raphson iteration will however yield more accurate positions of stagnation points over a wider range of gap size.

#### *Stagnation points not on $\theta = 0$*

Figures 3–6 show that in addition to the central stagnation points there is a variable number of ‘side’ stagnation points which lie away from the  $\theta = 0$  line. The position of these points can be determined by an adaptation of the bisection method described

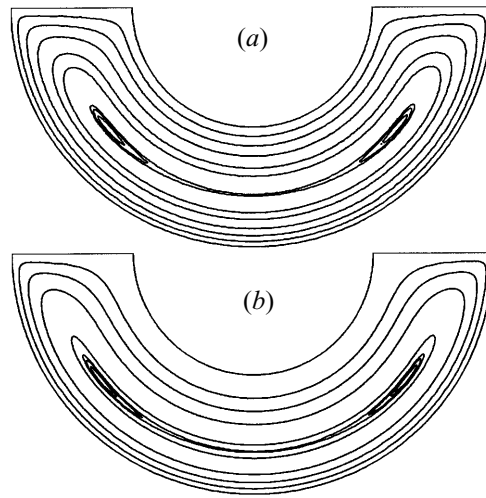


FIGURE 4. Streamline patterns for  $\bar{R} = 0.5$ : (a)  $S = -0.5$ ; (b)  $S = 0$ .

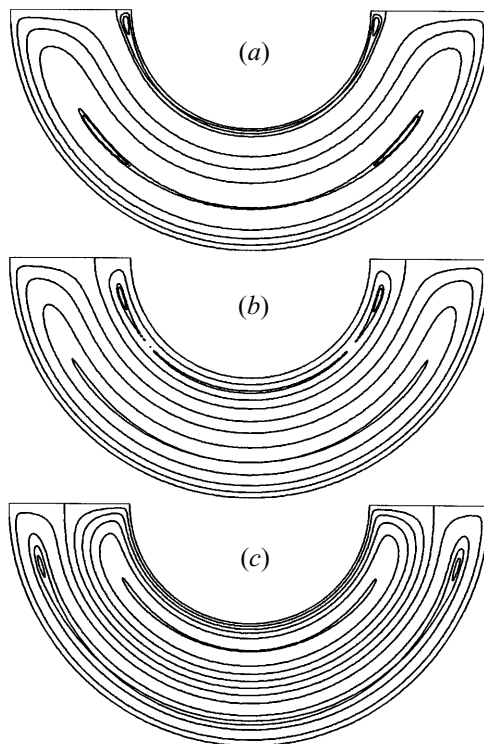


FIGURE 5. Streamline patterns for  $\bar{R} = 0.5$  and  $S \in (0, 2]$ :  
 (a)  $S = 0.1$ ; (b)  $S = 0.5$ ; (c)  $S = 2.0$ .

above. The domain is divided into a polar grid, so that each segment contains at most one stagnation point. The velocity components (2.3) can then be used to determine which segments contain a stagnation point and iterative bisection gives their position. Since the number of stagnation points is not known *a priori*, results must be checked against those from a finer grid.

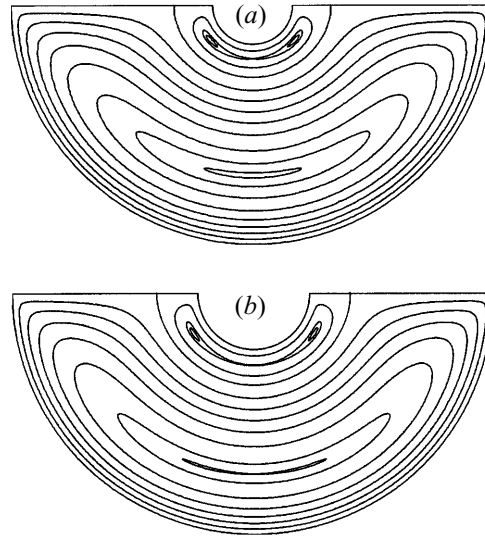


FIGURE 6. Streamline patterns for  $S = 0.5$ : (a)  $\bar{R} = 0.167$ ; (b)  $\bar{R} = 0.222$ .

### 3.4. Classification of stagnation points

The stagnation points found in the previous section can be described as either elliptic (centre points) or hyperbolic (saddle points) depending on the structure of the flow close to them. To determine the nature of a particular stagnation point it is possible to expand (3.6) as a Taylor series about that point. Suppose there is a stagnation point at  $r = a$ ,  $\theta = 0$ , then changing to coordinates  $x = a\theta$ ,  $y = a - r$ , with origin at the stagnation point, (3.6) takes the form

$$\psi = \sum_{n=1}^{\infty} Y_n(y) \cos(2n-1) \frac{x}{a}.$$

Expanding each eigenfunction about  $x = 0$ ,  $y = 0$ :

$$Y_n(y) = Y_n(0) + y \left. \frac{dY_n}{dy} \right|_{y=0} + \frac{1}{2} y^2 \left. \frac{d^2 Y_n}{dy^2} \right|_{y=0} + \dots,$$

$$\cos(2n-1) \frac{x}{a} = 1 - (2n-1)^2 \frac{x^2}{2a^2} + \dots,$$

then

$$\psi = \alpha + \epsilon y + \beta x^2 + \gamma y^2 + O(y^3), \quad (3.10)$$

where

$$\alpha = \sum_{n=1}^{\infty} Y_n(0), \quad \beta = -\frac{1}{2a^2} \sum_{n=1}^{\infty} (2n-1)^2 Y_n(0),$$

$$\epsilon = \sum_{n=1}^{\infty} \left. \frac{dY_n}{dy} \right|_0, \quad \gamma = \frac{1}{2} \sum_{n=1}^{\infty} \left. \frac{d^2 Y_n}{dy^2} \right|_0.$$

The  $\epsilon$  term is the azimuthal component of velocity at the stagnation point and should therefore be zero. However, since the position of the stagnation point is found numerically  $\epsilon$  is always non-zero – in fact it is of order  $10^{-18}$ . As the radial separation of stagnation points (for  $S > 0$ ) is much greater than this error in their positions the

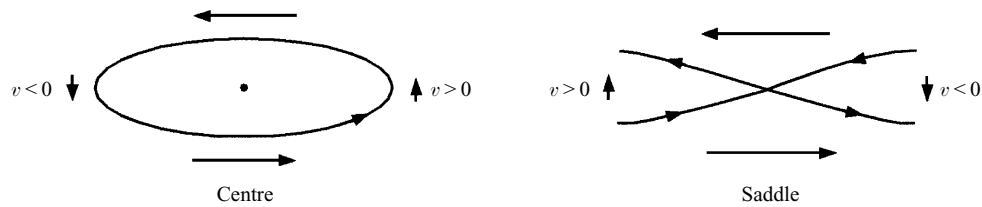


FIGURE 7. Direction of flow near a centre and a saddle point. The sign of  $v$  changes at a bifurcation.

$\epsilon$  term does not affect their classification. Setting  $\psi = \text{constant}$  in (3.10), it is seen that when  $\beta$  and  $\gamma$  have the same sign the streamlines are ellipses centred at  $(0, -\epsilon)$  indicating that the stagnation point is a centre. Similarly, when  $\beta$  and  $\gamma$  are opposite in sign the streamlines are hyperbolae and the stagnation point is a saddle point. Since  $\beta$  and  $\gamma$  depend on  $\bar{R}$  and  $S$  there are critical values of those parameters where the stagnation point changes from a centre to a saddle or vice versa.

Figure 7 shows a centre and a saddle point and indicates the direction of flow near each. As the flow is shear dominated, one would expect that at a bifurcation only the vertical (radial) component of velocity changes sign and since close to the stagnation point the velocity is given by  $(u, v) \approx (2\gamma y, -2\beta x)$ , this corresponds to a change in the sign of  $\beta$ . Indeed computations show that  $\beta$  changes sign while  $\gamma$  increases monotonically with  $\bar{R}$ .

## 4. Results and discussion

### 4.1. Streamline patterns

Figure 3 shows examples of streamline plots for three different values of radius ratio,  $\bar{R}$ . The speed ratio is fixed at  $S = -1$ , at which value the cylinders move with equal peripheral speed in opposite directions. In all three cases the flow consists of a large recirculatory pattern, symmetric about  $\theta = 0$ , with a stagnation point on the centreline. For small  $\bar{R}$ , figure 3(a), this stagnation point is elliptic, and no further features are visible in the flow.

However, at a larger radius ratio, figure 3(b), the main recirculation contains two sub-eddies, a separatrix, and a saddle point on the line  $\theta = 0$ . Clearly a bifurcation in the flow has occurred at some critical value of  $\bar{R}$  resulting in a change of type at the stagnation point on  $\theta = 0$  and the generation of two new 'stagnation points' on either side. This flow structure was also observed in the solid-walled cavities considered by Krasnopolskaya *et al.* (1996) and Gurcan (1996), who showed that the strongest of the corner eddies present when  $S = 0$  immediately transform into two free eddies connected by a saddle point when  $S$  is made non-zero.

Another bifurcation occurs at a higher value of  $\bar{R}$ , giving rise to a third sub-eddy, see figure 3(c). The occurrence of this bifurcation and flow structure was first identified by Gurcan (1996) and subsequently by Kelmanson & Lonsdale (1996) as part of a mechanism by which a double-eddy structure is transformed into a single eddy. It will be shown that in the current problem many more stagnation points and sub-eddies are generated as  $\bar{R} \rightarrow 1$ .

In figure 3(b), where  $\bar{R} = 0.5$  and  $S = -1$ , the stagnation point on  $\theta = 0$  is situated approximately halfway between the cylinders. As  $S$  approaches zero it moves outwards (figure 4), but there is no change in the qualitative structure of the flow,

even when  $S = 0$  – the Moffatt eddies seen in the cavity with rigid walls do not appear here. There is also no change in structure as speed ratio is made more negative.

As  $S$  increases above zero a second recirculation grows (figure 5a) so that the flow now exhibits two large recirculations and a dividing streamline. Each main recirculation also displays a substructure; figure 5(b) shows that the inner eddy contains three sub-eddies and two saddle points, whereas the outer one has two sub-eddies and a structure similar to that in figure 3(b). As speed ratio increases the separating streamline moves outwards as the inner eddy grows and at some critical speed ratio the two eddies will be comparable in size. At this value of  $S$  one would expect the structure of each eddy to be the same. If  $S$  is increased further the inner eddy becomes the larger, figure 5(c), resulting in a reversal of the flow structure in each eddy (compare figures 5b and 5c). This reversal is seen to be a general feature of the  $S > 0$  control space and allows the flow structure for large values of  $S$  to be inferred from those for small  $S$ . Changes in  $\bar{R}$  also cause a change in the substructure of each eddy, as illustrated by figure 6.

#### 4.2. Positions of central stagnation points

Figure 8 illustrates the difference between solutions of (3.8) and (3.9), for speed ratio  $S = -1$ , when there is only one stagnation point on  $\theta = 0$ . The dashed curve shows the position calculated from (3.8) while the dotted line was plotted using the solution of (3.9). It is clear that as  $\bar{R} \rightarrow 1$  the solution of (3.8) tends to that of (3.9) and, in fact, good agreement between the two exists for  $\bar{R} > 0.7$ . The solid curve in figure 8 shows the position of the stagnation point calculated using the bisection method. As  $\bar{R} \rightarrow 1$  this position tends to 0.5, as given by expression (3.9) above. For  $\bar{R} > 0.45$  the streamfunction-generated position agrees well with that from the small gap expression (3.8) but for smaller values of  $\bar{R}$  a clear difference exists between the two. This is attributable to the assumptions under which (3.8) was derived, namely that the flow in the core region is purely azimuthal. As the gap becomes larger this assumption becomes invalid and variations of the velocity field with  $\theta$  cannot be ignored.

A comparison of results for  $S = 1$  reveals that the streamfunction solution for each stagnation point position agrees well with the small gap solution over the whole range of  $\bar{R}$ . This is because there are two large recirculations of approximately equal thickness and hence the radial velocity component in the core region will remain negligible for smaller values of  $\bar{R}$  than is the case for  $S = -1$ . Another feature of this comparison is that the stagnation points are shifted inwards by the effect of curvature, not outwards as when  $S = -1$ . This suggests plotting stagnation point position as a function of speed ratio, as shown in figure 9 where, for  $S > 0$ , only the position of the outer stagnation point is plotted since its inner companion behaves in a very similar manner. On the scale shown the streamfunction and small gap solutions are indistinguishable, so the two curves displayed give the stagnation point position calculated from (3.9) and from the streamfunction. It is seen that the stagnation points are shifted inwards by the effect of curvature, except in a small region in the neighbourhood of  $S = -1$ . This is perhaps to be expected since the case  $S = -1$  is the only value of speed ratio for which there is no ‘Poiseuille contribution’,  $\partial p / \partial \theta = 0$ , and so one of the two curvature terms in (3.8) is identically zero. In fact  $p(r, \theta) = \text{constant}$  and the flow is effectively Couette flow for any radius ratio.

#### 4.3. Flow bifurcations

The term ‘flow bifurcation’ is used to describe a qualitative change in the structure of the flow as a result of stagnation points, located on  $\theta = 0$ , changing from a centre

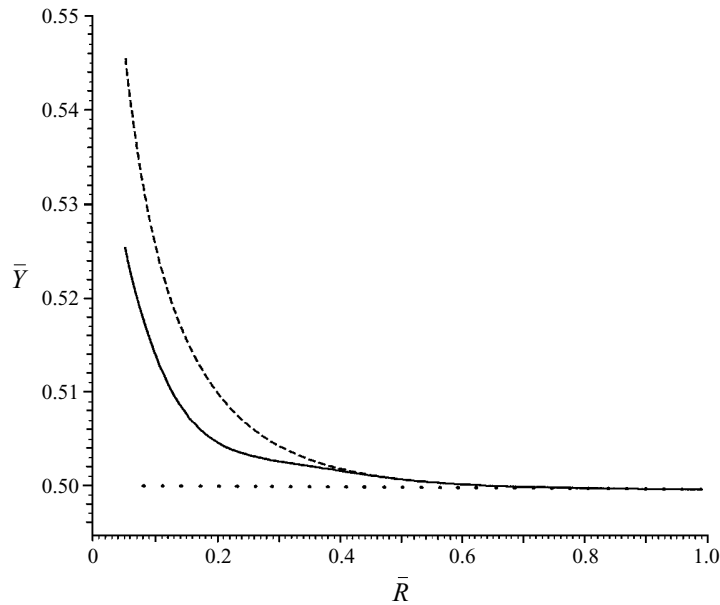


FIGURE 8. Radial position of stagnation point for  $S = -1$ :  
 ···, no curvature, (3.9); - - -, small gap, (3.8); —, streamfunction ( $\partial\psi/\partial r = 0$ ).

---

Radius ratio	Bifurcation
0.242	Centre → Saddle
0.546	Saddle → Centre
0.676	Centre → Saddle
0.716	Saddle → Centre
⋮	⋮

TABLE 2. Computed critical values of  $\bar{R}$  for  $S = -1$  and corresponding bifurcations for the stagnation point on  $\theta = 0$ .

---

to a saddle and vice versa. As discussed in §3.4 there are particular values of  $\bar{R}$  and  $S$  at which flow bifurcations occur. Taking a specific case, when  $S = -1$ , the critical values of  $\bar{R}$  are given in table 2 where the first four bifurcations are shown.

Table 2 and the sequence of plots in figure 3 indicate that, as  $\bar{R}$  increases, each successive bifurcation at  $(x, y) = (0, 0)$  causes a change in the type of stagnation point on  $\theta = 0$  together with the generation of two additional stagnation points on either side of  $(0, 0)$  whose angular separation increases with  $\bar{R}$ . It has been suggested that this repeated sequence by which more stagnation points are born could be proven by functional analytic methods and clearly this is a matter for further investigation. The scenario of a centre stagnation point becoming a saddle and the birth of two centres can be shown graphically by plotting the angular location of the points,  $\theta$ , against  $\bar{R}$ . Figure 10 shows such a plot for  $S = -1$  where centres are given by solid and saddles by dashed lines; there is a clear sequence of what would be termed ‘pitchfork’ bifurcations.

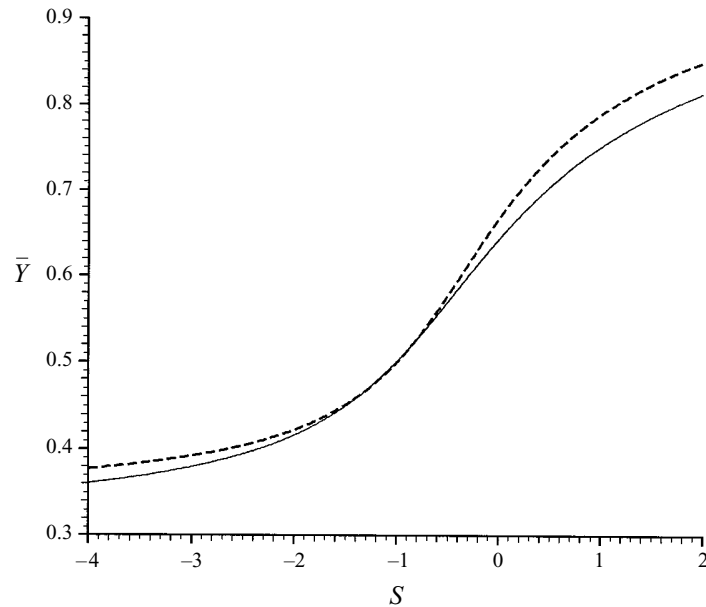


FIGURE 9. Variation of stagnation point position with speed ratio for  $\bar{R} = 0.5$ :  
 - - -, no curvature, (3.9); —, streamfunction ( $\partial\psi/\partial r = 0$ ).

#### 4.4. Local flow structure

Knowing the number and type of stagnation points in the domain is not always sufficient to determine the structure of the flow. When there are five or fewer stagnation points the structure is obvious since there is only one way to connect the points in a symmetrical pattern (as already seen in figures 3–6). However, once there are more than five stagnation points there are a number of alternatives, as shown in figure 11, and, due to the limited resolution of computer graphics, it is difficult to generate streamline plots of sufficient accuracy to determine the topology visually.

At first glance schematic (*d*) in figure 11 might seem to be the correct continuation of the pattern, but closer inspection reveals that for the flow to change continuously from pattern (*c*), as  $\bar{R}$  is increased, only pattern (*e*) is possible. This can be shown by examining the streamfunction value at each stagnation point. For example consider the three options for seven stagnation points shown in figure 11. In the first case (schematic *d*) all the saddle points lie on the same streamline and hence would have the same value of  $\psi$ . Similarly the third structure would imply that the value of  $|\psi|$  at the central stagnation point would be lower than that at any other. Table 3 shows that pattern (*e*) is indeed the correct structure since the streamfunction values at the saddle points (asterisked) indicate that  $\psi$  is more negative at the inner saddle point than at the others (compare graph (*e*), showing  $|\psi|$  against  $\theta$ , in figure 11).

Thus a pattern emerges: as  $\bar{R}$  is increased, the first two flow bifurcations lead to a separatrix enclosing three sub-eddies (shown schematically as (*c*) in figure 11) and the next results in the birth of a new separatrix within the central part of the first (schematic *e*). A further flow bifurcation leads to a pattern where the inner separatrix has the same structure as that enclosing it (schematic *h*) and at this stage the second separatrix is 'complete'. Computations suggest that subsequent bifurcations generate and develop a sequence of separatrices within its central section.

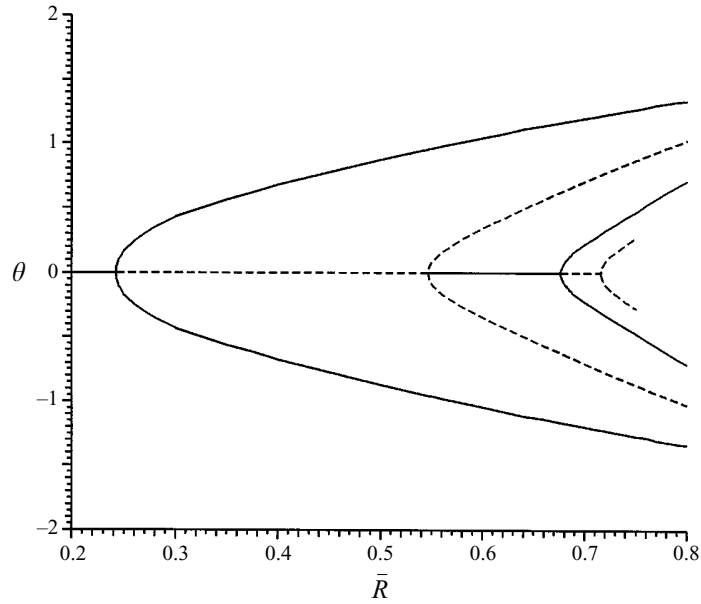


FIGURE 10. Flow bifurcation diagram for  $S = -1$  illustrating a sequence of pitchfork bifurcations: —, centres; ---, saddles.

$\bar{R} = 0.70$		$\bar{R} = 0.71$		$\bar{R} = 0.72$	
$\theta$	$\psi/(1 - \bar{R})$	$\theta$	$\psi/(1 - \bar{R})$	$\theta$	$\psi/(1 - \bar{R})$
-1.19658	-0.2511353655	-1.21171	-0.2511792473	-1.22604	-0.2512207323
-0.70449	-0.2493327921*	-0.73819	-0.2493843802*	-0.77154	-0.2494332062
-0.21288	-0.2493381739	-0.26441	-0.2493897119	-0.31147	-0.2494384911
0.00000	-0.2493381630*	0.00000	-0.2493896981*	-0.05602	-0.2494384765
0.21288	-0.2493381739	0.26441	-0.2493897119	0.05602	-0.2494384765
0.70449	-0.2493327921*	0.73819	-0.2493843802*	0.31147	-0.2494384911
1.19658	-0.2511353655	1.21171	-0.2511792473	0.77154	-0.2494332062
				1.22604	-0.2512207323

TABLE 3. Values of  $\psi/(1 - \bar{R})$  at stagnation points for  $S = -1$ . The scaling  $(1 - \bar{R})$  is used to compare  $\psi$ -values with expression (4.2) which is based on a gap width of unity.

This bifurcation pattern is consistent with the argument that the flow, as  $\bar{R} \rightarrow 1$ , should tend to unidirectional shear flow. Taking for simplicity the case  $S = -1$ , the velocity distribution (3.9) reduces to

$$v(\bar{Y}) = 2\bar{Y} - 1 \tag{4.1}$$

which features a stagnation line at  $\bar{Y} = 1/2$ . The flux between the upper boundary and the stagnation line can be found by integration:

$$\psi_{\text{stag}} = \int_0^{1/2} (2\bar{Y} - 1)d\bar{Y} = -\frac{1}{4}. \tag{4.2}$$

Correcting for the scaling of the domain, table 3 shows that, as  $\bar{R}$  increases, the

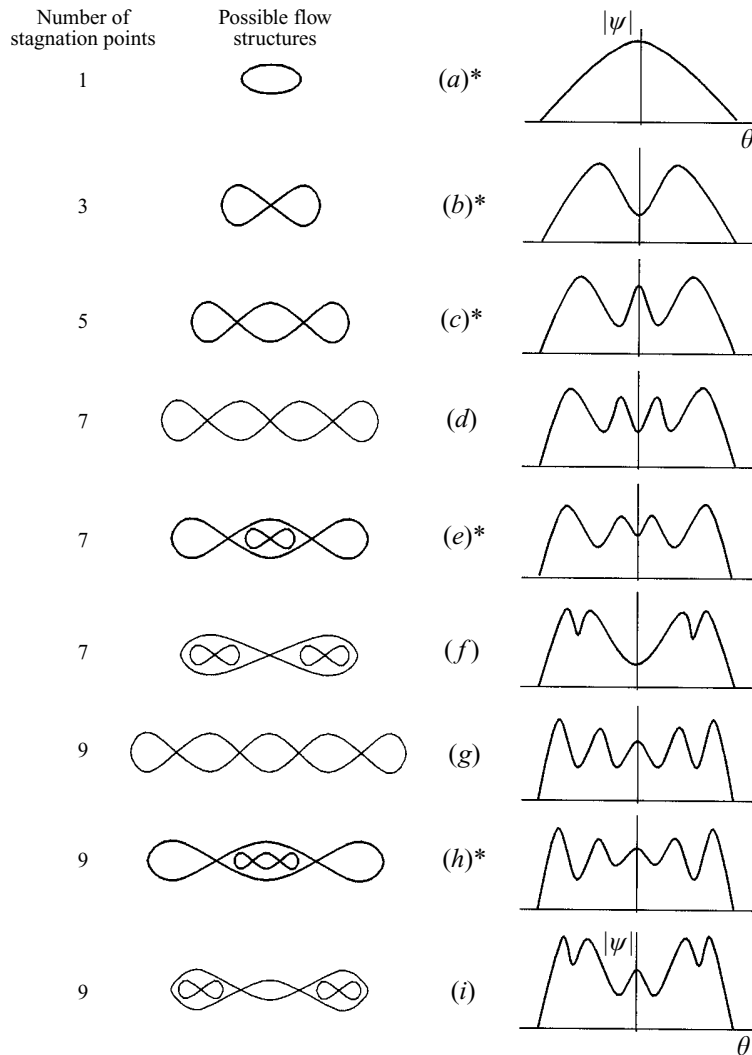


FIGURE 11. Possible flow patterns for given numbers of stagnation points. The actual flow patterns are asterisked. All the stagnation points lie at approximately the same radius (the outermost ones are shifted inwards slightly) and the graphs to the right show  $|\psi|$  against  $\theta$  at that radius. Note that maxima and minima correspond to centres and saddles respectively.

computed value of  $\psi$  at the central stagnation point approaches this limit value. This suggests two possible reasons for the sequence of bifurcations as  $\bar{R} \rightarrow 1$ : to generate stagnation points approximating a stagnation line; and to enable the streamfunction, on that line and in the central region, to approach the value for unidirectional shear flow.

Close to a stagnation point, the vorticity is  $\omega = -2(\beta + \gamma)$  where  $\beta$  and  $\gamma$  are the coefficients in expression (3.10). Since  $\gamma$  is always larger than  $\beta$  the vorticity at each stagnation point is of the same sign. In fact as  $\bar{R}$  increases,  $\gamma$  becomes much larger than  $\beta$ , reflecting the long thin nature of the sub-eddies, and so the vorticity can be approximated by  $\omega \approx -2\gamma$ . To compare with shear flow the velocity distribution (4.1)

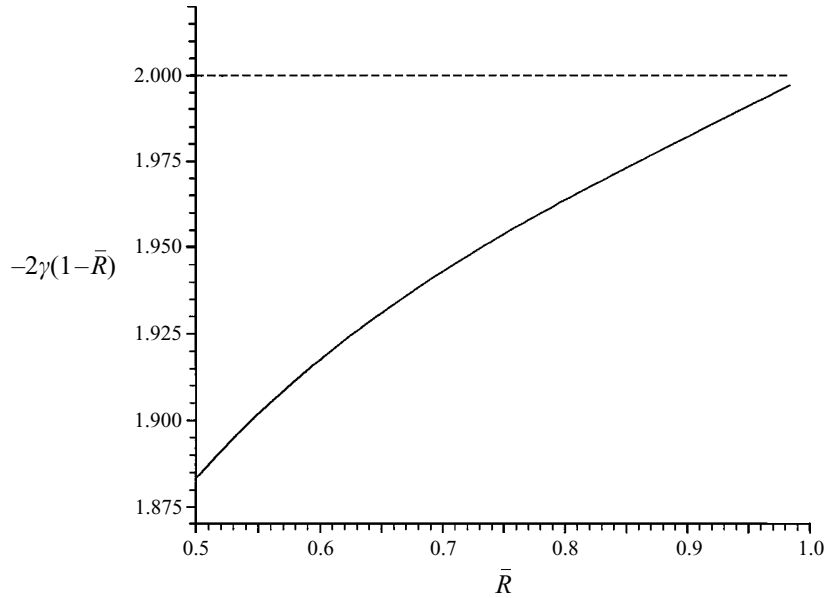


FIGURE 12. Plot of vorticity against radius ratio for  $S = -1$ :  
 - - -, shear flow value,  $\omega_{\text{shear}}(1 - \bar{R})$ ; —,  $-2\gamma(1 - \bar{R})$ .

for a constant gap width of unity is rewritten in terms of a gap of height  $1 - \bar{R}$ ,

$$v(r) = \frac{2r}{1 - \bar{R}} - \frac{1 + \bar{R}}{1 - \bar{R}},$$

giving the shear flow vorticity

$$\omega_{\text{shear}} = \frac{dv}{dr} = \frac{2}{1 - \bar{R}}.$$

Figure 12 shows a plot of  $\omega_{\text{shear}}(1 - \bar{R})$  and  $-2\gamma(1 - \bar{R})$  against  $\bar{R}$  and demonstrates clearly that as  $\bar{R} \rightarrow 1$ , the vorticity tends to  $\omega_{\text{shear}}$ , supporting the above argument that the flow is approximating simple shear.

#### 4.5. Control-space diagram

Flow bifurcations can be tracked either by fixing the speed ratio and varying the geometry, as in the previous illustration, or by fixing the geometry and varying the speed ratio. Rather than use  $\bar{R}$ , a cavity aspect ratio,  $H$ , defined by

$$H = \frac{1 - \bar{R}}{\bar{R}},$$

is taken as the geometry parameter so as to facilitate comparison with other authors. The effect of variations in both  $H$  and  $S$  can be visualized in a parameter-space diagram. For  $S \leq 0$ , figure 13 shows a sequence of bifurcation curves,  $\eta_1, \eta_2, \eta_3, \eta_4, \dots$  which, apart from the first, have negligible variation with  $S$ . They divide the space into a number of regions,  $\alpha_1, \alpha_2, \alpha_3, \dots$ , in each of which the flow structure near the stagnation point on  $\theta = 0$ , and also the total number of stagnation points, is identified by an appropriate schematic. Typical streamline plots for regions  $\alpha_1, \alpha_2, \alpha_3$  are given in figures 3(a), 3(b), 3(c) respectively.

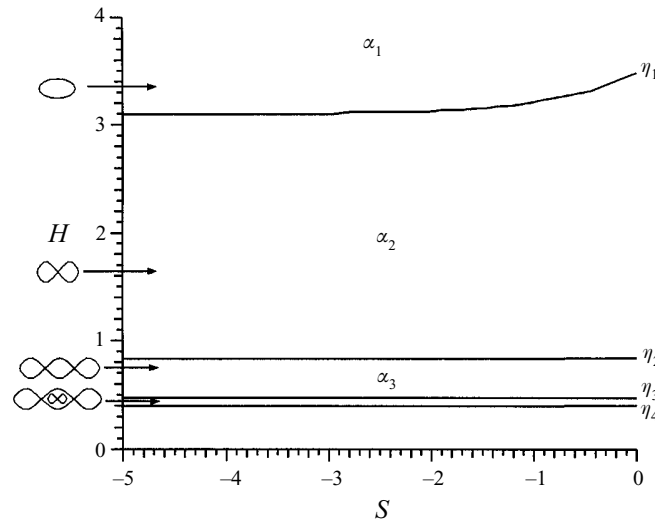


FIGURE 13. Control-space diagram for cylindrical cavity with  $S \leq 0$ : the schematics on the left indicate the flow structure near the stagnation point on  $\theta = 0$  and the total number of stagnation points in  $-\pi/2 \leq \theta \leq \pi/2$ .

For  $S > 0$  the cylinders co-rotate giving rise to two large eddies, each with a stagnation point lying on  $\theta = 0$ . Flow bifurcations may arise at different parameter values within each large eddy and in figure 14 the dashed and solid curves refer to bifurcations in the inner and outer eddies respectively. Again parameter space is divided into a number of distinct regions where typical flow structures in each of the 'large eddies' is illustrated by a two-part schematic, the upper and lower parts referring to the inner and outer eddies respectively. For large aspect ratios the speed ratio has a marked effect on the structure of the flow but as  $H$  decreases, the influence of  $S$  is restricted to a small range of values centred on  $S = 1$ . In this region the bifurcation curves produce a pattern which repeats and diminishes in size as  $H \rightarrow 0$ . Away from  $S = 1$  the bifurcation curves for small  $H$  are similar to those for  $S < 0$ .

Points A and B are where dashed and solid curves intersect and bifurcations of the same type arise simultaneously in the inner and outer eddies. A symmetry argument might suggest that A and B should lie on  $S = 1$  as is the case with a rectangular cavity which, for  $S = 1$ , has two recirculations of equal thickness and symmetrical about a dividing streamline (Gurcan 1996). In fact the coordinates of A and B are  $(S, H) = (0.960, 6.519)$  and  $(0.998, 1.222)$  respectively, and so both points are displaced slightly from the line  $S = 1$ . Hence, in the cylindrical cavity, curvature introduces asymmetric effects which are more noticeable for large aspect ratios, when the difference in the radii of the cylinders is greater. In general the effects of curvature are expected to diminish as  $\bar{R} \rightarrow 1$ , i.e.  $H \rightarrow 0$ . This is evident in figures 13 and 14, where the bifurcation curves as  $H \rightarrow 0$  are similar to those for a rectangular cavity, Gurcan (1996).

The streamline plots in figure 5 all have radius ratio  $\bar{R} = 0.5$ , which is equivalent to  $H = 1$ . Figure 5(b) has  $(S, H) = (0.5, 1)$  and so portrays the flow in region  $\beta_3$  of figure 14, showing that the upper eddy has three sub-eddies and two saddles, while the lower one exhibits two sub-eddies located symmetrically about a single saddle on the line  $\theta = 0$ . Figure 5(c) illustrates the flow for region  $\beta_4$  of figure 14 and shows

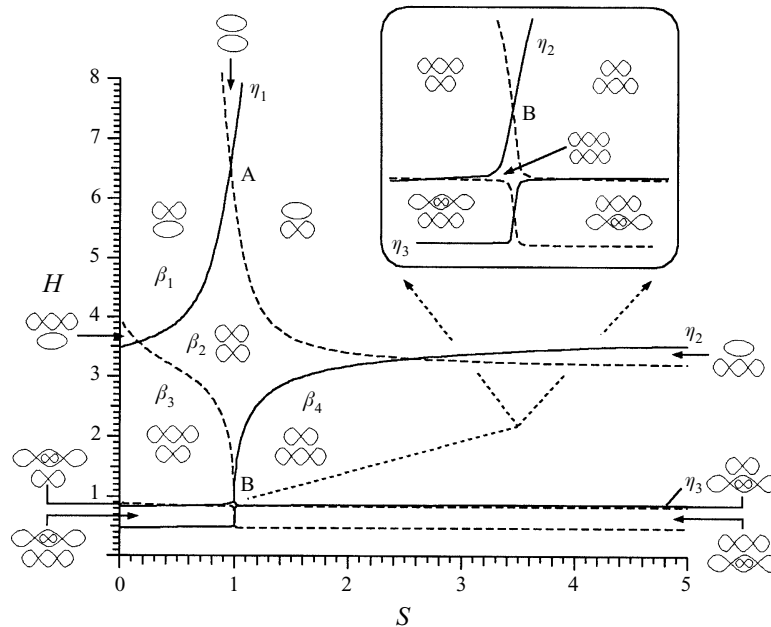


FIGURE 14. Control space diagram for  $S > 0$ : - - -, flow bifurcation curve for the top (inner) eddy; —, flow bifurcation curve for the bottom (outer) eddy. The flow structure near stagnation points on  $\theta = 0$  and the number of stagnation points in each large recirculation are shown schematically for each region defined by the bifurcation curves. The insert is a magnified view of the region close to B ( $S \approx 1$ ).

that the structure is the inverse of that in region  $\beta_3$ . Figures 6(a) and 6(b) have  $(S, H) = (0.5, 5)$  and  $(0.5, 3.5)$  and correspond to regions  $\beta_1$  and  $\beta_2$  respectively.

As  $S \rightarrow 0$  the inner recirculation diminishes, figure 4(a), and eventually disappears – unlike the rigid-walled cavity (Gurcan 1996; Krasnopolskaya, *et al* 1996) where it transforms into corner eddies. The outer recirculation remains as  $S \rightarrow 0$  and the (solid) bifurcation curves associated with it meet at  $S = 0$  with those from  $S < 0$ . The reader will note that the dashed bifurcation curves never reach  $S = 0$  since the inner eddy vanishes there.

As for application of this work, coating processes – as mentioned in the introduction – are an obvious candidate since recirculations tend to be ubiquitous, especially in roll coating. Indeed a knowledge of flow bifurcations arising from variations in aspect ratio and speed ratio will be particularly useful to those who seek to obtain finite element solutions for velocity fields in thin-film, free-surface coating flows.

M. Wilson is grateful to the EPSRC for provision of a studentship. Sincere thanks are also due to the referee for a critical appraisal of the assumptions of the model.

#### REFERENCES

- BENDER, C. M. & ORSZAG, S. 1978 *Advanced Mathematical Methods for Scientists and Engineers*. McGraw-Hill, International student edition.
- BREWSTER, D. B., GROSBERG, P. & NISSAN, A. H. 1959 The stability of viscous flow between horizontal concentric cylinders. *Proc. R. Soc. Lond. A* **251**, 76–91.
- CHEN, F. & CHANG, M. H. 1992 Stability of Taylor-Dean flow in a small gap between rotating cylinders. *J. Fluid Mech.* **243**, 443–455.

- CHEN, K. S., KU, A. C., CHAN, T. M. & YANG, S. Z. 1990 Flow in the half-filled annulus between horizontal concentric cylinders in relative motion. *J. Fluid Mech.* **213**, 149–169.
- COUETTE, M. 1890 Etudes sur le frottement des liquides. *Ann. Chim. Phys.* **21**, 433–510.
- DEAN, W. R. 1928 Fluid motion in a curved channel. *Proc. R. Soc. Lond. A* **121**, 402.
- GASKELL, P. H., INNES, G. E. & SAVAGE, M. D. 1997 An experimental investigation of meniscus roll coating. *J. Fluid Mech.* In press.
- GASKELL, P. H., SAVAGE, M. D., SUMMERS, J. L. & THOMPSON, H. M. 1995 Modelling and analysis of meniscus roll coating. *J. Fluid Mech.* **298**, 113–137.
- GURCAN, F. 1996 Flow bifurcations in rectangular, lid-driven cavity flows. PhD Thesis, University of Leeds.
- JANA, S. C., METCALFE, G. & OTTINO, J. M. 1994 Experimental and computational studies of mixing in complex Stokes flows: the vortex mixing flow and multicellular flow. *J. Fluid Mech.* **269**, 199–246.
- JEFFREY, D. J. & SHERWOOD, J. D. 1980 Streamline patterns and eddies in low-Reynolds-number flow. *J. Fluid Mech.* **96**, 315–334.
- JOSEPH, D. D. & STURGES, L. 1978 The convergence of Biorthogonal Series for biharmonic and Stokes flow edge problem. *SIAM J. Appl. Maths* **34**, 7–26.
- KELMANSON, M. A., & LONSDALE, B. 1996 Eddy genesis in the double-lid-driven cavity. *Q. J. Mech. Appl. Maths* **49**, 635–655.
- KOMODA, A. Y. 1983 An outline of new electro-galvanizing line (KMRCEL). *Kawasaki Steel Tech. Rep.* **8**, 17–27.
- KRASNOPOLSKAYA, T. S., MELESHKO, V. V., PETERS, G. W. M. & MEIJER, H. E. H. 1996 Steady Stokes flow in an annular cavity. *Q. J. Mech. Appl. Maths* **49**, 593–619.
- MOFFATT, H. K. 1964 Viscous and resistive eddies near a sharp corner. *J. Fluid Mech.* **18**, 1–18.
- MUTABAZI, I. & ANDERECK, C. D. 1991 Transition from time-dependent to stationary flow patterns in the Taylor-Dean system. *Phys. Rev. A* **44**, 6169–6172.
- MUTABAZI, I., HEGSETH, J. J., ANDERECK, C. D. & WESFREID, J. E. 1988 Pattern formation in the flow between two horizontal coaxial cylinders with a partially filled gap. *Phys. Rev. A* **38**, 4752–4760.
- MUTABAZI, I., NORMAND, C., PEERHOSSAINI, H. & WESFREID, J. E. 1989 Oscillatory modes in the flow between two horizontal corotating cylinders with a partially filled gap. *Phys. Rev. A* **39**, 763–771.
- NABATAME, M. 1984 An outline of Fukuyama No.3 electrolytic galvanizing line. *Nippon Kokan Tech. Rep. (overseas)* **40**, 9–16.
- NORMAND, C., MUTABAZI, I. & WESFREID, J. E. 1991 Recirculation eddies in the flow between two horizontal coaxial cylinders with a partially filled gap. *Eur. J. Mech. B/Fluids* **10**, 335–348.
- PAN, F. & ACRIOS, A. 1967 Steady flows in rectangular cavities. *J. Fluid Mech.* **28**, 643–655.
- SHANKAR, P. N. 1993 The eddy structure in Stokes flow in a cavity. *J. Fluid Mech.* **250**, 371–383.
- TAYLOR, G. I. 1923 Stability of a viscous liquid contained between two rotating cylinders. *Phil. Trans. R. Soc. Lond. A* **223**, 289–343.
- THOMPSON, H.M. 1992 A theoretical investigation of roll coating phenomena. PhD Thesis, University of Leeds.